Research Square

Preprints are preliminary reports that have not undergone peer review.
They should not be considered conclusive, used to inform clinical practice,
or referenced by the media as validated information.

Bioinspired light-driven water surface jumper with record high jumping performance that transcends the biological jumping limit

metin sitti

msitti@ku.edu.tr

Koç University

Changsong Zhan

Soochow University

Zhen Hou

Soochow University

Zhaomin Chen

Soochow University

Naizheng Tan

Nanhai Institute of Harbin Engineering University, Sanya 572024, China.

Jiwei jiang

Soochow University

Binchi Zhang

State Key Laboratory of Bioinspired Interfacial Materials Science, Jiangsu Key Laboratory for Carbon-based Functional Materials and Devices and Institute of Functional Nano and Soft Materials (FUNSO

Chenjun Chu

State Key Laboratory of Bioinspired Interfacial Materials Science, Jiangsu Key Laboratory for Carbon-based Functional Materials and Devices and Institute of Functional Nano and Soft Materials (FUNSO

A-Man Zhang

Harbin Engineering University

Hui Zhang

State Key Laboratory of Bioinspired Interfacial Materials Science, Jiangsu Key Laboratory for Carbon-based Functional Materials and Devices and Institute of Functional Nano and Soft Materials (FUNSO

Bin Dong

Soochow University https://orcid.org/0000-0001-5681-372X

Lifeng Chi

Soochow University https://orcid.org/0000-0003-3835-2776

Article

Keywords:

Posted Date: April 17th, 2026

DOI: https://doi.org/10.21203/rs.3.rs-9292421/v1

License: This work is licensed under a Creative Commons Attribution 4.0 International License. Read Full License

Additional Declarations: There is **NO** Competing Interest.

Bioinspired light-driven water surface jumper with record high jumping performance that transcends the biological jumping limit

Changsong Zhan[1,2,†], Zhen Hou[1,†], Zhaomin Chen[1,3,†], Naizheng Tan[4,†], Jiwei Jiang[1,†,*], Binchi Zhang[1], Chenjun Chu[1], A-Man Zhang[4,5], Hui Zhang[1,*], Bin Dong[1,*], Lifeng Chi[1,*], Metin Sitti[3,*]

[1]State Key Laboratory of Bioinspired Interfacial Materials Science, Jiangsu Key Laboratory for Carbon-based Functional Materials and Devices and Institute of Functional Nano and Soft Materials (FUNSOM), Soochow University, Suzhou 215123, China.

[2]Suzhou Laboratory, Suzhou 215123, China.

[3]School of Medicine and College of Engineering, Koç University, 34450 Istanbul, Turkey.

[4]Nanhai Institute of Harbin Engineering University, Sanya 572024, China.

[5]College of Shipbuilding Engineering, Harbin Engineering University, 150001 Harbin, China.

[†]These authors contributed equally to this work: Changsong Zhan, Zhen Hou, Zhaomin Chen, Naizheng Tan, Jiwei Jiang.

*Corresponding authors. E-mail: msitti@ku.edu.tr; chilf@suda.edu.cn; bdong@suda.edu.cn; huizhang@suda.edu.cn; jwjiang@suda.edu.cn

Abstract: Artificial water surface jumpers hold great promises in a variety of application fields. However, it is still challenging to achieve a jumping performance that transcends the biological limit because the typical jumping processes involve deformation and the internal energy dissipation during the deformation processes often leads to low performances. Herein, inspired by the snapping shrimp, we report a tailor-designed, light-driven water surface jumper with a record-high jumping height (~910 body length), which is far superior to that of the best biological counterpart (~18 body length in case of pygmy mole crickets). The jumping process features an ultrafast take-off velocity (~14.9 m/s), a fast response time (~0.5 ms) and a high energy conversion efficiency (2.12%). The extraordinary jumping performance relies on a fundamentally different mechanism other than deformation that harnesses the synergy between the photothermal effect of the methyl-substituted polypyrrole nanoparticle constituent, the trapped air inside the surface micropores and the high stiffness of the jumper to generate high-pressure bubble and realize efficient propulsion. The excellent jumping performance and weight-carrying capability (~36 times of the jumper's weight), together with the controllability over both jumping direction and height, make the light-driven water surface jumper reported in the current study potentially attractive for soft robotics and sensing applications.

Introduction

Jumping is the ability of many living creatures to suddenly increase the speed of their locomotion in order to prey, escape from predators, traverse complex terrains or leap onto hosts[1-4]. Inspired by nature, great efforts have been exerted to the development of artificial counterparts with similar jumping capabilities. The jumping behavior empowers these artificial jumpers with excellent obstacle-crossing capabilities[5-8], making them attractive for a wide range of applications ranging from search and rescue missions[9], environmental exploration to detection[10,11] and medical devices[12,13]. Among different artificial jumpers, those with the ability to jump on the surface of water have received more and more attention in recent years. These jumpers have direct contact with the water environment and could move from one water area to another by jumping. This unique property thus makes the water surface jumpers particularly attractive for aquatic environmental monitoring[14], water cleaning[15], and sensing applications[16].

Aiming to achieve better jumping performances, a variety of water surface jumpers, including the small-scale water jumping robot[17], the jumping robotic insect[18], the miniature water surface jumping robot[19], the large-scale water jumping robot[20], and the soft jumping robot[21], have been developed based on different types of advanced materials including elastomers[22], shape-memory alloys[17], piezoelectrics[23], hydrogels[15], and composites[19,24]. Under the electrical[18,23,24], magnetic[21], light[15,25] or mechanical[26] stimulation, material or structural deformation occurs in these water surface jumpers which provides the driving force for the jumping behavior. Up till now, a jumping height as high as 18 times of the jumper's own body length (BL) has been realized[15],

which is comparable to that of the best animal jumper (i.e. pygmy mole crickets[27], 18 BL). In order to achieve such jumping height, mechanisms involving deformation are normally required. However, the limitation in the internal energy dissipation during the deformation process has constrained the jumping performance, thus hindering its potential applications in various fields. It still remains a challenge to achieve a jumping performance that transcends the biological jumping limit.

In this work, inspired by the snapping shrimp, we report a light-driven water surface jumper with record high jumping performance that far transcends the biological limit (Fig. 1a,b). It can achieve a jumping height as high as 910 times of its body length (BL), which is ~51 times of that of the best biological counterpart (~18 BL in case of pygmy mole crickets), with a fast response time (~0.5 ms) and a high take-off speed (~14.9 m/s). The jumper is composed of binary components, i.e. methyl-substituted polypyrrole (Me-PPy) nanoparticle and crosslinked polyvinyl alcohol (PVA), and has micropores on its surface. It is operated based on a mechanism which is fundamentally different from the deformation process, i.e. it harnesses the synergistic interaction between the photothermal Me-PPy nanoparticles, the trapped air inside the surface micropores and the high stiffness to generate high-pressure bubble and achieve efficient propulsion. The excellent jumping performance enables the light-driven water surface jumper to carry a cargo which is ~36 times of its own weight. This, together with the well-controlled jumping direction and height, makes this jumper attractive for a variety of applications. As a proof-of-the-concept, we have demonstrated its potentials in mobile and distributed water sensing.

Results

Fabrication and characterization of the light-driven water surface jumper. The light-driven water surface jumper consists of binary components, i.e., Me-PPy in the form of nanoparticles (as can be seen from Supplementary Fig. 1) and PVA, which is fabricated based on oxidative polymerization (Supplementary Fig. 2) and breath-figure method[28,29] (Fig. 1c). Among others, Me-PPy nanoparticles are chosen due to their excellent photothermal property[30,31], while PVA is selected because it could function as a stiff polymeric film-forming agent[32]. The light-driven jumper has a typical size of 800 μm × 800 μm × 100 μm (length × width × thickness) (Supplementary Fig. 3) with micropores on one side of its surface. The micropores are formed by applying volatile solvents onto the polymeric film under the humid condition (i.e. breath figure method, Fig. 1c). As can be seen from the scanning electron microscope (SEM) images shown in Fig. 1d,e, the micropore has an average diameter of 64 μm (Supplementary Fig. 4) and a depth of 16 μm (Fig. 1e inset), respectively. Note that the surface micropores are crucial for the bubble generation and the propulsion of the jumper. In addition, we have studied the surface morphology of the areas other than the micropores. As shown in the SEM (Supplementary Fig. 5) and the atomic force microscopy (AFM) images (Supplementary Fig. 6), these areas are smooth with a root mean square roughness (RMS) of approximately 0.64 nm. The composition of the light-driven jumper is studied by the energy-dispersive X-ray (EDX) analysis and Fourier transform infrared spectroscopy (FTIR). Among others, the EDX analysis (Supplementary Fig. 7) shows that the nitrogen (the characteristic element from Me-PPy) and oxygen (the

characteristic element of PVA) elements distribute uniformly throughout the film, thus confirming the presence of both Me-PPy and PVA. Furthermore, as shown in the FTIR spectra (Supplementary Fig. 8), the characteristic peaks originating from Me-PPy (red curve, bands at 1071 cm^{-1} and 2932 cm^{-1} derive from the C-N stretching vibration and the asymmetric stretching vibration of the $-CH_3$ group, respectively) and PVA (blue curve, bands at 3325 cm^{-1} and 932 cm^{-1} originate from the stretching vibration of the O-H bond and the in-plane bending vibration of CH-OH group, respectively) can be observed in the Me-PPy/PVA jumper (black curve), further indicating the presence of both constituents. In addition, the ultraviolet visible near-infrared (UV-Vis-NIR) spectrum shown in Supplementary Fig. 9 black curve reveals that the Me-PPy/PVA composite exhibits a wide absorption peak in the NIR region which is likely due to the absorption of the Me-PPy constituent (the pristine PVA shows negligible absorption in this spectral range, Supplementary Fig. 9 red curve). This shows that the Me-PPy/PVA jumper may be able to absorb NIR light and convert it to the thermal energy, which lays the foundation for its photothermal actuation. The surface of the Me-PPy/PVA jumper with micropores has a water contact angle of 112.25° (Supplementary Fig. 10) which is higher than that of the hydrophobic Me-PPy/PVA film without micropores (Supplementary Fig. 11) and the water droplet on a vertically aligned jumper surface does not roll off (Supplementary Fig. 12). These, together with the partial wetting of the surface micropores (Supplementary Fig. 13), indicate the surface wetting state is between the Wenzel and Cassie states. Moreover, the Me-PPy/PVA film has a Young's modulus of ~1850 MPa and an ultimate strength of ~96 MPa (Supplementary Fig. 14,

red curve), indicating it is non-elastic and hard in nature. The higher Young's modulus and ultimate strength as compared to those of crosslinked PVA (The Young's modulus and ultimate strength are ~555 MPa and ~41 MPa, respectively, Supplementary Fig. 14 black curve) are likely because the presence of Me-PPy nanoparticles enhances the mechanical strength of the composite by acting as reinforcement fillers[33].

The jumping behavior of the light-driven water surface jumper. The light-driven jumper can achieve the jumping motion on the surface of water. When the center area of the jumper's bottom surface (the side with micropores) is illuminated by the near-infrared (NIR) light (1.4 W/cm^2), it jumps from the water surface into the air, as indicated in Supplementary Fig. 15 and Supplementary Movie 1. The light-driven jumper excels in both take-off velocity and jumping height. Among others, as can be seen from Fig. 1f, the jumper, within a fast response time of 0.5 ms, shows an ultra-fast take-off velocity of 14.9 m/s (i.e. 18625 BL/s, which is obtained through the motion analysis). This is more than 164 times faster than the maximum take-off velocity of the best water surface jumper reported to date (which is less than 113 BL/s)[34]. The fast response time and ultra-fast take-off velocity lay the foundation for its high jumping performance on the water surface. The water surface jumper could achieve a jumping height of approximately 910 BL (72.8 cm in height) (Fig. 1g and Supplementary Movie 2). We have surveyed the jumping performance of the biological water surface jumpers and the artificial counterparts. As summarized in Fig. 1h,i and Supplementary Fig. 16, the best jumping performance the biological[27] or the artificial jumpers[15] reported to date can achieve is ~18 BL. The water surface jumper reported in the current study thus far

transcends the biological jumping limit and sets a new record of water surface jumping performance. In addition, as illustrated in Fig. 1b and Supplementary Movie 2, the light-driven water surface jumper exhibits the typical parabolic trajectory and the speed of the jumper starts to decrease after the actuation due to the influence of the gravitational force.

The jumping mechanism of the light-driven water surface jumper. The water surface jumping behavior of the light-driven jumper is possibly due to the photothermal effect of the Me-PPy component and the subsequent water vaporization, bubble formation and propulsion (Fig. 2a-f). We have investigated the water surface jumping mechanism by examining the initial jumping process, the role of surface micropores and the PVA component, the gas bubble-jumper interaction and the temperature changes using high-speed camera, control experiments, computer simulation and thermal imaging, respectively.

Among others, as can be seen from the high-speed camera images indicated in Fig. 2g-j and the corresponding movie (Supplementary Movie 3), a light-induced bubble is formed at the water-jumper interface within an extremely short period of time (~5 μs) and the bubble expands swiftly during 45 μs. This process is similar to the bubbles formed by snapping shrimps through rapid claw snapping[35]. Note that, due to the surface wetting state between the Wenzel and Cassie states (Supplementary Fig. 13), the air trapped inside the micropores could serve as the heterogeneous nucleating site for the water gas bubble to nucleate and the heterogeneous nucleation is advantageous over homogeneous one in terms of bubble formation because it can significantly reduce

the degree of superheating[36]. This is evidenced by the fact that the jumpers without the surface micropores only shows low jumping performances (Supplementary Fig. 17). The jumper stays on the water surface until the bubble starts to burst at approximately 50 μs, which provides the driving force for the jumping behavior as evidenced by the departure of the jumper from the surface of water. After departure, the jumper shows negligible shape changes (Supplementary Fig. 15) which is likely due to its high stiffness (Supplementary Fig. 14). The high stiffness may avoid the energy dissipation due to the deformation, thus facilitating the jumping performance. This is further proved by the fact that the softer jumpers (made of Me-PPy/Gelatin or Me-PPy/ Hydroxypropyl cellulose (HPC)) which exhibit deformation after departure (Supplementary Fig. 18) show much lower jumping performance (lower jumping height, take-off speed and slower response time, Supplementary Fig. 19).

In order to acquire more information during this initial jumping process, we have developed a three-dimensional (3D) bubble-jumper model and utilized the OpenFOAM software to simulate the light-induced bubble behavior and the pressure applied onto the jumper during the light-driven jumping process. As shown in Fig. 2k-n, after the nucleation of the gas bubble, its volume rapidly expands until it partially ruptures at about 50 μs. On the other hand, as can be seen from the pressure-time relationship shown in Supplementary Fig. 20, the pressure exerted by the bubble on the model jumper peaks at ~50 μs and it could reach ~8.3 MPa which is 83 atm, a value substantially higher than those reported previously in similar systems[37]. This high pressure could thus provide sufficient propulsion force for the jumping motion after the

bubble bursting. Note that the continuous increase of the bubble volume in water after 50 μs is likely due to the inertia-driven expansion of the bubble following pressure release (Fig. 2j,n).

Furthermore, we have monitored the temperature changes during the jumping process. As can be seen from Fig. 2o,p, the temperature of the jumper rises from 24.4 °C to 164.3 °C during the jumping process which exceeds the boiling point of water (100 °C), thereby laying the foundation of the water vaporization at the jumper and water interface. The increase of the temperature of the jumper under the light irradiation is possibly because of the photothermal effect of the Me-PPy component inside the jumper. Under NIR light irradiation, the electrons of Me-PPy are excited from the highest occupied molecular orbital (HOMO) to the lowest unoccupied molecular orbital (LUMO). The photoexcited electrons relax back to the ground state through nonradiative relaxation (i.e. the electron-vibration coupling), resulting in the generation of heat[38].

Based on the above observations, we propose the following tentative mechanism of the light-driven jumper: Under the light irradiation, the surface temperature of the light-driven jumper increases rapidly above the boiling point of water, which results in the water vaporization. The water gas bubble utilizes the air inside the micropores as the nucleation center, resulting in the formation of a high-pressure bubble at the bottom surface of the jumper. The bubble burst and the pressure relief at ~50 μs provide the direct propulsion force. The high stiffness of the Me-PPy nanoparticle reinforced PVA

composite film facilitates the efficient energy transfer from the bubble to the jumper, resulting in high jumping performance.

We have studied the force to propel the light-driven jumper according to the Newton's equation as follows:

$$F_{\text{jump}} = m\left(\frac{v_{\text{j}}}{t_{\text{j}}}\right) + G \quad (1)$$

where F_{jump} is the driving force for jumping, G is gravity, which is 1.47 μN for the current light-driven jumper with a mass (m) of 1.5×10^{-7} kg, v_{j} is the take-off velocity of the light-driven jumper (14.9 m/s), and t_{j} is the acceleration time (~25 μs). The driving force of the light-driven jumper is calculated based on Eq. (1) to be ~90.9 mN.

On the other hand, the propulsion force (F_{jump}) could also be estimated based on the pressure using the following equation:

$$F_{\text{jump}} = \iint P(r)\,\mathrm{d}A \quad (2)$$

where A denotes the pressure application area on the surface of the jumper, r is the distance between the measurement point and the center of the model jumper, and $P(r)$ is the pressure at a given distance. $P(r)$ can be obtained by fitting the pressure measurements at points (Supplementary Fig. 21), i.e., $P(r) = 8189917.54835 \times e^{-r/1.72668\times10^{-5}} + 123815.67931$ (Supplementary Fig. 22). The propulsion force can thus be calculated to be 96.7 mN, which is close to that calculated based on Eq. (1) (90.9 mN), thus indicating that the pressure applied on the jumper by the bubble is likely the driving force for the water surface jumping.

In addition, we have examined the thermal stability of the light-driven jumper. As can be seen from the thermogravimetric analysis (TGA) shown in Supplementary Fig.

23, the degradation temperature of the light-driven jumper is around 200 °C, which indicates that it is thermally stable during the actuation process (164.3 °C, Fig. 2p). Moreover, we have examined the morphology of the jumper after the light actuation. As shown in Supplementary Fig. 24, there are negligible changes of the surface morphology. The thermal and morphological stability, together with the negligible shape deformation after jumping (Supplementary Fig. 15), lays the foundation for the repetitive light actuation. As illustrated in Supplementary Fig. 25, the light-driven jumper could be repeatedly actuated for multiple times without deterioration in the jumping performance, revealing its excellent reusability.

Motion control of the light-driven water surface jumper. We have first studied the influence of the material composition, size, thickness, pore size of the light-driven jumper on the jumping performance. We then realize the control over the jumping direction and the jumping trajectory by adjusting the irradiation light intensity and irradiation position.

Among others, the water surface jumping behavior of the light-driven jumper (including the response time, the take-off velocity and the jumping height) relies on the photothermal effect of the substituted PPy component, which is closely related to its energy gap. We have examined the jumping performance, the photothermal temperature of the substituted PPy/PVA based jumper and the energy gap of PPy with different substituent groups. Note that the PVA content inside the jumper remains unchanged. As summarized in Supplementary Table 1, the methyl substituted PPy (Me-PPy) exhibits the best jumping performance (higher jumping height, faster response

time and take-off speed) due to its narrower energy gap and higher photothermal temperature. On the other hand, the molecular weight of Me-PPy also has an effect on the jumping performance. As depicted in Supplementary Fig. 26, the high molecular weight Me-PPy shows the improved response time, take-off velocity and jumping height because the increased number of conjugated π bonds leads to the decreased energy gap and thus stronger photothermal effect (Supplementary Fig. 27). We thus select the high molecular weight Me-PPy as the photothermal agent in the current study.

The jumping behavior is also highly dependent on the content of Me-PPy inside the jumper. As can be seen from Supplementary Fig. 28, the Me-PPy content needs to be high enough (≥6 wt%) to generate the photothermal effect required for actuation. The response time decreases with the increasing Me-PPy content (Supplementary Fig. 28a). The take-off velocity and the jumping height reach the maximum when the concentration of Me-PPy is around 18 wt% (Supplementary Fig. 28b,c). However, if too much Me-PPy (>18 wt%) is present, the decreased mechanical property (Supplementary Fig. 29) leads to low performances because of the deformation during the jumping process (Supplementary Fig. 30). Furthermore, we have evaluated the effect of the thickness and size of the light-driven jumper on the jumping behavior. As shown in Supplementary Fig. 31,32, the optimal thickness and size are approximately 100 μm and 800 μm × 800 μm (length × width), respectively. The thicker and larger light-driven jumpers increase the overall weight of the jumper, leading to longer response time, lower take-off velocity and lower jumping height. While for smaller jumpers, it could not generate sufficient photothermal effect for the jumping motion.

And for thinner jumper, the jumper is prone to deformation during the jumping process which is unfavorable for the jumping performance. The optimum Me-PPy content, thickness and size are thus 18 wt%, 100 μm and 800 μm × 800 μm (length × width), respectively. Additionally, the micropores on the surface of the light-driven jumper are of great importance to its jumping behavior. As shown in Supplementary Fig. 33,34, the pore size has to be moderate (~64 μm) for the jumper to achieve a high take-off speed and jumping height. This is because the suitable pore size allows the formation of the surface wetting state between Wenzel and Cassie states (Supplementary Fig. 35) which facilitates the bubble nucleation.

In order to realize the motion control, we have studied the influence of light intensity and irradiation position on the jumping behavior. Among others, as can be seen from Supplementary Fig. 36, the response time, the take-off velocity and the jumping height become better with the increasing light intensity. This is likely because more heat could be generated through photothermal conversion which facilitates faster response and the generation of stronger propulsion forces. Note that the light intensity should be kept below 1.6 W/cm^2 otherwise the light-driven jumper could be damaged. Furthermore, as shown in Fig. 3a-e and Supplementary Movie 4, when the left half of the jumper is illuminated, it jumps to the right direction. This is likely because the propulsion force is generated at the irradiation position where the gas bubble is formed (as shown in Fig. 3d) and its deviation from the mass center of the jumper leads to the jumping behavior toward the right direction (as can be seen from the force analysis shown in Fig. 3a inset). As the illumination position progresses to the center of the

jumper, the take-off angle (α) (the angle between the take-off direction and the horizontal direction) gradually increases (Fig. 3f red curve to black curve and Supplementary Fig. 37), resulting in different jumping heights and landing distances (Fig. 3f). On the contrary, when the right half of the jumper is irradiated, it could jump to the left (Fig. 3g-k and Supplementary Movie 5) with distinguishable jumping trajectories and landing distances which are controlled by the illumination location (Fig. 3l). Therefore, it is possible to control the jumping trajectories and the landing distances of the jumper by manipulating the irradiation intensity and position. Note that the water surface jumping behavior of the light-driven jumper could also be realized when light is applied from the top of the jumper (Supplementary Fig. 38).

Potential application demonstration of the light-driven water surface jumper. In this part, we have first constructed an artificial water strider based on the light-driven jumper. Then, we fabricate a hybrid light-driven jumper by coating Me-PPy/PVA composite onto the shell of a water flea. Third, as a proof-of-the-concept, we have demonstrated the potential of the light-driven jumper as a mobile sensor for monitoring environmental temperature at different locations. Fourth, we also explore its potential in distributed colorimetric sensing for collective water-quality detection.

Water strider is a semi-aquatic arthropod that possesses the ability to rapidly and efficiently jump on the water surface, which facilitates its exploration of new habitats, swift capture of food, and evasion of danger[2,39]. It has a typical body length of approximately 8-20 mm[40]. Inspired by nature, we have constructed an artificial water strider based on the light-driven jumper. As shown in Fig. 4a,b the artificial water

strider consisting of the Me-PPy/PVA composite has a size of 10 mm. And it could rapidly jump from the water surface under the light stimulation with a jumping height of ~50 cm (Fig. 4c and Supplementary Movie 6), which is ~50 BL (the natural water strider normally shows a jumping height of 10 BL)[40]. Note that only a small part (shown in the dotted circle in Supplementary Fig. 39) of this artificial water strider is irradiated which provides the propulsion force. When considering the irradiated part as an 'engine' while the rest as the 'cargo', the 'engine' could achieve a jumping height of 50 BL when carrying a 'cargo' which is ~18 times of its own weight. We have also evaluated the jumping performance of this artificial water strider when increasing the weight of the 'cargo' part. As indicated in Supplementary Fig. 40, the jumping performance decreases with the increasing weight, and the maximum weight the 'engine' part can carry to achieve the jumping behavior is approximately 36 times of its own weight. Based on this weight-carrying capability, we have fabricated a hybrid jumper by directly coating the shell of a water flea (2 mm in length) with the Me-PPy/PVA composite (Fig. 4d,e and Supplementary Fig. 41). The weight ratio between the shell of water flea (1.8 mg) and the Me-PPy/PVA coating (0.07 mg) is approximately 26 to 1. Under the stimulation of light, it can jump on the water surface with a jumping height of 36 cm (~180 BL) (Fig. 4f and Supplementary Movie 7). The jumping performance also depends on the weight of the hybrid jumper. As depicted in Supplementary Fig. 42, the jumping height decreases as the weight of the hybrid jumper increases. When considering the surface Me-PPy/PVA coating and the shell of water flea as the 'engine'

and ‘cargo’, respectively, the ‘engine’ could achieve a jumping behavior when carrying a maximum ‘cargo’ weight which is also around 36 times of that of the ‘engine’.

The excellent water surface jumping performance, together with the weight-carrying capability, makes the light-driven jumper in the current study attractive for water environment sensing applications. As a proof-of-the-concept example, we have explored its potential as a mobile sensor for monitoring environmental temperature at different locations. As shown in Supplementary Fig. 43a, we have loaded the light-driven jumper (the side without the micropores) (2 mm × 2 mm × 100 μm) with colorimetric temperature sensor (1 mm × 1 mm in size), which could be utilized to collect the temperature information (Supplementary Fig. 43b). We have also prepared a transparent container containing 12 water compartments (No. 1-12) with different temperatures and placed the light-driven jumper equipped with the colorimetric temperature sensor on the water surface of one compartment (No. 1, Fig. 4g,h). Upon light actuation, the jumper could jump to different compartments (No. 10 and 3) with the side containing the attached sensor facing up, which is likely due to the greater mass of the light-driven jumper compared with the on-board sensor. At each landing site, the color change of the on-board colorimetric sensor can be directly visualized through digital imaging, enabling the acquisition of environmental information (temperature) from each compartment (Fig. 4h-j). Unlike conventional temperature sensors, this jumper-based mobile sensing platform enables spatially resolved temperature monitoring across broad water surfaces, offering enhanced coverage, flexibility, and adaptability for environmental sensing applications.

Additionally, we have explored the potential of the jumpers as distributed colorimetric sensors for collective water environmental information collection. As indicated in Supplementary Fig. 44a,b, we have loaded the light-driven jumper (the side without the micropores) (2 mm × 2 mm × 100 μm) with colorimetric pH or water hardness sensors (1 mm × 1 mm in size), which could be utilized to collect the pH and water hardness information (Supplementary Fig. 44c,d and Supplementary Fig. 45). We have also prepared four water areas with low pH, high pH, low-hardness and high-hardness, respectively (Supplementary Fig. 46). 12 light-driven jumpers carrying different sensors are then actuated to jump toward different areas. At each location, the pH and water hardness information could be read out once the ions in the water diffuse throughout the jumper and induce the colour changes of the on-board colorimetric pH or water hardness sensors. Based on the digital imaging of the whole water area (as shown in Fig. 4k), the collective environmental information (the acidity and hardness distribution) from different areas could be simultaneously collected (Fig. 4l,m). Compared to conventional water environment sensors, distributed light-driven jumper-based sensors allow for simultaneous and collective water environmental sensing over a large area.

Discussion

A bio-inspired light-driven water surface jumper has been developed, which exhibits record-breaking jumping performance of ~910 BL (~51 times of that of the best insect jumper (18 BL)) with an ultrafast take-off velocity (~14.9 m/s), a fast response time (~0.5 ms) and a high conversion efficiency (2.12%). This jumper is

operated based on the synergistic interaction between the photothermal Me-PPy nanoparticles, the trapped air inside the surface micropores and the high material stiffness. And the following water vaporization, high-pressure bubble generation and propulsion provide the driving force for jumping. Both the jumping direction and height of the jumper could be well controlled by adjusting the irradiation intensity and position. This, together with the weight-carrying capability (~36 times of the jumper's weight), makes this jumper particularly attractive for water environmental monitoring. The light-driven water surface jumper proposed in the current study may not only help advance the design of jumpers with superior jumping performances but also set a new paradigm for applications in soft robotics and sensors.

Methods

Materials. Ferric chloride hexahydrate ($FeCl_3 \cdot 6H_2O$), PVA (molecular weight: 67 k), Gelatin, HPC, glutaraldehyde (GA, 50% aqueous solution), acetonitrile (≥ 99.5%), dimethyl sulfoxide (DMSO), dichloromethane (CH_2Cl_2), pyrrole and substituted pyrrole monomer (1-methylpyrrole, 1H-pyrrole-3-carbaldehyde, 1-phenylpyrrole, 2-acetylpyrrole, 1H-pyrrole-2-carbonitrile, 3-nitropyrrole) were purchased from Aladdin Company. All reagents were used directly without further purification. The colorimetric temperature sensor was obtained from Suzhou Han Electronic Materials Co., Ltd. The colorimetric pH and water hardness sensors were purchased from Sigma-Aldrich and Guangdong Huankai Microbial Sci. & Tech. Co., Ltd., respectively.

Preparation of Me-PPy nanoparticles. To prepare Me-PPy nanoparticles, 1.2 g of $FeCl_3 \cdot 6H_2O$ (the oxidant) were dissolved in 20 mL of deionized water (solution A). 213

μL of 1-methylpyrrole were mixed with 10 mL of deionized water for 10 min (solution B). Solution A was added to Solution B dropwisely to initiate the polymerization reaction, and the mixture was placed in an ice bath. After polymerization for 24 h, the Me-PPy nanoparticles inside the solution were filtered out and washed with deionized water for three times. The purified Me-PPy nanoparticles were then dispersed in 10 mL of deionized water. Me-PPy nanoparticles with 27 k, 28 k, and 30 k molecular weights were obtained by tuning the $FeCl_3$-to-monomer molar ratio to 1:1, 1.2:1 and 1.5:1, respectively. The polymerization temperature and time were kept at 25 °C and 12 h, respectively.

Preparation of Me-PPy/PVA film. 0.75 g of PVA were dissolved in 30 mL of deionized water at 90 °C (solution C). After complete dissolution, Me-PPy nanoparticle solution (10 mL) was added dropwisely to solution C. After mixing for 1 h, 0.2 mL of GA (1 wt%) was added and the mixture was stirred at 50 °C for 1 h. The mixture solution was dropcast onto a glass slide and placed under ambient condition for 12 h. The surface micropores were then fabricated using the breath figure method. In a typical experiment, the slide coated with surface composite film was immersed in a mixture of CH_2Cl_2 and DMSO solution (1:1) for 5 s and then transferred to a high humidity (~85%) environment. After placing there for 6 h, the composite film was peeled off from the glass slide, cut into different shapes and stored in an environment with a relative humidity of 20%. Different pore sizes were constructed by adjusting the CH_2Cl_2 to DMSO volume ratio and ambient humidity: increasing the ratio to 2:1 in ~75% humidity produced smaller pores of ~32 μm; decreasing the ratio to 1:2 at ~95%

humidity resulted in larger pores ~103 μm. The composite film containing Me-PPy derivatives and PVA was obtained in a fashion similar to that of Me-PPy/PVA except that pyrrole with various substituents (including nitro, carbonitrile, acetyl, phenyl, methyl, and aldehyde) was used as the monomer. In addition, the Me-PPy/Gelatin and Me-PPy/HPC films were fabricated in a similar way except gelatin or HPC was utilized instead of PVA.

Material characterization. SEM experiments were performed on a Hitachi SU8230 scanning electron microscope with an EDX analysis accessory. Before SEM observation, the samples were sputtered with 8 nm thick gold. AFM measurements were performed on a Bruker Dimension Scanning Probe Microscope. Surface pore size and depth were determined by a Surface Profiler D-100. Young's modulus and ultimate strength were obtained by utilizing a tensile tester (34TM-50). Optical microscopic images were obtained by a Nikon Eclipse 80i microscope. CCD images and movies were captured by a Nikon Z7-II digital camera. The high-speed imaging was carried out using Phantom VEO710L-72GB. The captured videos were analyzed using the PhysVis software in order to obtain the response time, the motion trajectory and velocity. The water content inside the Me-PPy/PVA jumper was estimated by the oven-drying method, which was proximately 10 wt%. Unless otherwise mentioned, the Me-PPy and PVA contents inside the light-driven jumper were 18 wt% and 72 wt%, respectively. The motion of the jumper was activated by applying an 808 nm laser (High Tech Optoelectronics) which was placed 2 cm far from the jumper with an intensity of 1.4 W/cm^2. TGA was performed on a Mettler Toledo thermogravimetric analyzer. The

samples were placed on a platinum plate and heated from 25 °C to 600 °C at a rate of 10 °C/min in air. Infrared thermal images were obtained by a Fotric 289-H2000 camera. UV-Vis-NIR spectra were measured using a PerkinElmer Lambda 750/950 UV-Vis-NIR spectrophotometer. The energy gaps of different PPy samples were determined from the UV-Vis-NIR spectra using the Tauc plot method. Contact angle measurements were performed using a Data Physics OCA20 contact angle system. Gel permeation chromatography (GPC) was performed on a Waters 1515 system equipped with a Waters 2414 refractive index detector at 35 °C. Colorimetric sensors were attached to the surface of the jumpers by using PVA (1 μL of 1 wt% PVA solution) as the glue.

Simulation of the bubble growth process and the bubble pressure. To investigate the bubble dynamics induced by light irradiation, we have modeled bubble growth and pressure profiles using combined potential flow theory and the Navier-Stokes equations. Bubble shape evolution was derived using Keller's equation, which was adapted by Zhang for compressible fluids[41]:

$$\left(\frac{C-\dot{R}}{R}+\frac{\mathrm{d}}{\mathrm{d}t}\right)\left(\frac{R}{C-\dot{R}}\frac{\mathrm{d}F}{\mathrm{d}t}\right)=2R\dot{R}^2+R^2\ddot{R} \tag{3}$$

where C is the speed of sound in the compressible fluid medium, R, $\dot{R}$ and $\ddot{R}$ represent the bubble radius, the expansion velocity, and acceleration, respectively, and F corresponds to the combination of bubble pulsation force, migration force, and environmental force. Expand to get the following formula:

$$\left(1+\frac{\dot{R}}{C}\right)H+\frac{R}{C}\dot{H}+\frac{1}{4}\left(1+\frac{\dot{R}}{C}\right)|\vec{v}|^2+\frac{R}{2C}|\vec{v}|\left|\dot{\vec{v}}\right|=\frac{3}{2}\left(1-\frac{\dot{R}}{3C}\right)\dot{R}^2+\left(1-\frac{\dot{R}}{C}\right)R\ddot{R} \tag{4}$$

where H is the pressure difference between the inside and outside of the bubble and $\vec{v}$ is the migration velocity.

For the migration dynamics of the bubble, we used the following equation:

$$C_{\mathrm{a}}R\dot{\vec{v}}+\left(3C_{\mathrm{a}}\dot{R}+\dot{C}_{\mathrm{a}}R\right)\vec{v}+\frac{R}{\rho}\nabla P_{\mathrm{a}}+\frac{3}{8}C_{\mathrm{d}}\vec{v}|\vec{v}|=0 \tag{5}$$

where C_{a} is the additional mass coefficient of the fluid, C_{d} is the drag coefficient of the fluid, and P_{a} is the pressure field in the surrounding fluid. To handle boundary effects due to the bubble's proximity to a rigid plate, we applied the mirror image method by introducing a virtual bubble to simulate the boundary interaction. The time-history of the bubble radius is governed by two initial parameters: the initial radius R_0 and the initial pressure difference across the bubble wall H_0. Assuming an initial internal bubble pressure of P_0 = 169 MPa and an ambient pressure of P_∞, the initial pressure difference is obtained as $H_0 = P_0 - P_\infty$. With H_0 known, the initial radius R_0 was subsequently inferred by fitting the experimentally recorded radius-time curve of the bubble. Simulations were conducted in OpenFOAM with a fixed thin-film boundary above the bubble which represented a non-deformable surface. Pressure measurement points were placed at fixed positions on the plate surface to capture pressure data during bubble expansion and interactions with the boundary (Supplementary Fig. 17).

Calculations of optical energy input, kinetic energy output, and energy conversion efficiency.

The input energy (from NIR light) could be calculated by:

$$P_{\mathrm{NIR}}=I\times A \tag{6}$$

$$E_{\mathrm{input}}=P_{\mathrm{NIR}}\times t \tag{7}$$

where P_{NIR} is the power of the applied laser, I is the power density (1.4 W/cm^2), A is the irradiation area (A = 2.8 × 10^{-3} cm^2), E_{input} is the input energy, t is the laser

irradiation time (~0.2 s) before the light-driven jumper takes off, and E_{input} is calculated to be ~784 μJ.

And the kinetic energy at the moment of take-off could be be obtained by:

$$E_{jump}=\frac{1}{2}mv^2 \quad (8)$$

where m is the mass of the light-driven jumper, which is 0.15 mg, and v is the take-off velocity (14.9 m/s). The kinetic energy is estimated to be ~16.65 μJ.

The energy conversion efficiency (η) could thus be estimated to be 2.12%:

$$\eta=\frac{E_{jump}}{E_{input}}=2.12\% \ . \quad (9)$$

Data availability

All data that support the finding of the current study are available from the corresponding author upon request.

Acknowledgments:

This work is supported by National Natural Science Foundation of China (22573070, 52503158), Basic Research Program of Jiangsu (BK20250795), Joint International Research Laboratory of Carbon Based Functional Materials and Devices, Key Projects of the Regional Joint Fund of the National Natural Science Foundation of China (U24A20496), the Gusu Innovation and Entrepreneurship Talent Program-Major Innovation Team (ZXD2023002), the Suzhou Key Laboratory of Functional Nano & Soft Materials, Collaborative Innovation Center of Suzhou Nano Science & Technology, the 111 Project, and Suzhou Key Laboratory of Functional Nano & Soft Materials. It is also supported by the Priority Academic Program Development of Jiangsu Higher Education Institutions (PAPD), the Fund for Excellent Creative

Research Teams of Jiangsu Higher Education Institutions and Suzhou Key Laboratory of Surface and Interface Intelligent Matter (SZS2022011).

Author contributions:

C.S.Z., Z.H., Z.M.C., J.W.J., H.Z. B.D., L.F.C., and M.S. proposed and designed the research. C.S.Z., Z.H., Z.M.C., J.W.J. and B.C.Z. performed the experiments and analyzed the data. N.Z.T. and A.M.Z. performed the bubble simulation. C.S.Z. and N.Z.T. conducted the model analysis. A.M.Z., J.W.J., H.Z., B.D., L.F.C. and M.S. supervised the research. All authors discussed the results and wrote the manuscript.

Competing interests:

The authors declare no competing interests.

Additional information

Supplementary information associated with this paper can be found in the online version.

Publisher's note Springer Nature remains neutral about jurisdictional claims in published maps and institutional affiliations.

References

1. Goettler, C., Elflein, K., Siegwart, R. & Sitti, M. Spider origami: Folding principle of jumping spider leg joints for bioinspired fluidic actuators. *Adv. Sci.* **8**, 2003890 (2021).
2. Yang, E. J., Son, J. H., Lee, S. I., Jablonski, P. G. & Kim, H.Y. Water striders adjust leg movement speed to optimize takeoff velocity for their morphology. *Nat. Commun.* **7**, 13698 (2016).

3. Rothschild, M., Schlein, Y., Parker, K. & Sternberg, S. Jump of the oriental rat flea xenopsylla cheopis (Roths.). *Nature* **239**, 45-48 (1972).

4. Burrows, M. Froghopper insects leap to new heights. *Nature* **424**, 509-509 (2003).

5. Chen, R., et al. Legless soft robots capable of rapid, continuous, and steered jumping. *Nat. Commun.* **12**, 7028 (2021).

6. Ramirez Serrano, F., Hyun, N. P., Steinhardt, E., Lechère, P. L. & Wood, R. J. A springtail-inspired multimodal walking-jumping microrobot. *Sci. Adv.* **10**, eadp7854 (2025).

7. Yim, J. K., Wang, E. K., Lee, S. D., Hunt, N. H., Full, R. J. & Fearing, R.S. Monopedal robot branch-to-branch leaping and landing inspired by squirrel balance control. *Sci. Adv.* **10**, eadq1949 (2025).

8. Hawkes, E.W., et al. Engineered jumpers overcome biological limits via work multiplication. *Nature* **604**, 657-661 (2022).

9. Wang, Y., et al. Insect-scale jumping robots enabled by a dynamic buckling cascade. *Proc. Natl. Acad. Sci. U.S.A.* **120**, e2210651120 (2023).

10. Li, M., Wang, X., Dong, B. & Sitti, M. In-air fast response and high-speed jumping and rolling of a light-driven hydrogel actuator. *Nat. Commun.* **11**, 3988 (2020).

11. Kumar, S., et al. Reversible kink instability drives ultrafast jumping in nematodes and soft robots. *Sci. Adv.* **10**, eadq3121 (2025).

12. Hu, W., Lum, G. Z., Mastrangeli, M. & Sitti, M. Small-scale soft-bodied robot with multimodal locomotion. *Nature* **554**, 81-85 (2018).

13. Karacakol, A. C., Alapan, Y., Demir, S. O. & Sitti, M. Data-driven design of shape-programmable magnetic soft materials. *Nat. Commun.* **16**, 2946 (2025).

14. Zhang, T., Dong, J., Chen, Q., Wu, X., Wang, S. & Guan, Y. Review of bioinspired aquatic jumping robots. *Biomimetic Intell. Rob.* **5**, 100204 (2025).

15. Wang, X., et al. Beyond surface tension-dominated water surface jumping. *Nat. Commun.* **16**, 3034 (2025).

16. Zufferey, R., et al. Consecutive aquatic jump-gliding with water-reactive fuel. *Sci. Robot.* **4**, eaax7330 (2019).

17. Shin, B., Kim, H. Y. & Cho, K. J. Towards a biologically inspired small-scale water jumping robot. 2*008 2nd IEEE RAS & EMBS International Conference on Biomedical Robotics and Biomechatronics*, 127-131 (2008).

18. Koh, J. S., et al. Jumping on water: Surface tension-dominated jumping of water striders and robotic insects. *Science* **349**, 517-521 (2015).

19. Jiang, F., Zhao, J., Kota, A. K., Xi, N., Mutka, M. W. & Xiao, L. A miniature water surface jumping robot. *IEEE Robot. Autom. Lett.* **2**, 1272-1279 (2017).

20. Yan, J., Yang, K., Zhang, X., Zhang, X. & Zhao, J. A new type large-scale water-jumping robot design and simulation. *2018 IEEE International Conference on Real-time Computing and Robotics (RCAR)*, 177-182 (2018).

21. Wang, Y. B., Du, X. Z., Zhang, H. M., Zou, Q., Law, J. & Yu, J. F. Amphibious miniature soft jumping robot with on-demand in-flight maneuver. *Adv. Sci.* **10**, 2207493 (2023).

22. Hu, D. L., Chan, B. & Bush, J. W. M. The hydrodynamics of water strider locomotion. *Nature* **424**, 663-666 (2003).

23. Chen, Y. F., et al. A biologically inspired, flapping-wing, hybrid aerial-aquatic microrobot. *Sci. Robot.* **2**, eaao5619 (2017).

24. Yang, K., Liu, G., Yan, J., Wang, T., Zhang, X. & Zhao, J. A water-walking robot mimicking the jumping abilities of water striders. *Bioinspir. Biomim.* **11**, 066002 (2016).

25. Xiang, Y., et al. Toward a multifunctional light-driven biomimetic mudskipper-like robot for various application Scenarios. *ACS Appl. Mater. Interfaces* **14**, 20291-20302 (2022).

26. Yu, J., Su, Z., Wu, Z. & Tan, M. Development of a fast-swimming dolphin robot capable of leaping. *IEEE-ASME Trans. Mechatron.* **21**, 2307-2316 (2016).

27. Burrows, M. & Sutton, G. P. Pygmy mole crickets jump from water. *Curr. Biol.* **22**, R990-R991 (2012).

28. Widawski, G., Rawiso, M. & François, B. Self-organized honeycomb morphology of star-polymer polystyrene films. *Nature* 369, 387-389 (1994).

29. Zhang, A., Bai, H. & Li, L. Breath figure: A nature-inspired preparation method for ordered porous films. *Chem. Rev.* **115**, 9801-9868 (2015).

30. Hao, L., Dong, C. & Yu, D. Polypyrrole derivatives: Preparation, properties and application. *Polymers* **16**, 2233 (2024).

31. Wang, X., Liu, Q., Wu, S., Xu, B. & Xu, H. Multilayer polypyrrole nanosheets with self-organized surface structures for flexible and efficient solar-thermal Energy conversion. *Adv. Mater.* **31**, 1807716 (2019).

32. Wu, S.W., et al. Poly(vinyl alcohol) hydrogels with broad-range tunable mechanical properties via the Hofmeister effect. *Adv. Mater.* **33**, 2007829 (2021).

33. Weng, M., et al. Multi-functional actuators made with biomass-based graphene-polymer films for intelligent gesture recognition and multi-mode self-powered sensing. *Adv. Sci.* **11**, 2309846 (2024).

34. Gwon, M., Kim, D., Kim, B., Han, S., Kang, D. & Koh, J. S. Scale dependence in hydrodynamic regime for jumping on water. *Nat. Commun.* **14**, 1473 (2023).

35. Lohse, D., Schmitz, B. & Versluis, M. Snapping shrimp make flashing bubbles. *Nature* **413**, 477-478 (2001).

36. Gallo, M., Magaletti, F., Georgoulas, A., Marengo, M., De Coninck, J. & Casciola, C. M. A nanoscale view of the origin of boiling and its dynamics. *Nat. Commun.* **14**, 6428 (2023).

37. Gonzalez-Avila, S. R., Nguyen, D. M., Arunachalam, S., Domingues, E. M., Mishra, H. & Ohl, C. D. Mitigating cavitation erosion using biomimetic gas-entrapping microtextured surfaces (GEMS). *Sci. Adv.* **6**, eaax6192 (2020).

38. Yang, S., et al. A critical perspective on photothermal de-icing. *Adv. Mater.* **37**, 2415237 (2025).

39. Kim, W., et al. Two different jumping mechanisms of water striders are determined by body size. *Proc. Natl. Acad. Sci. U.S.A.* **120**, e2219972120 (2023).

40. Kim, W., et al. Physics of sliding on water explains morphological and behavioural allometry across a wide range of body sizes in water striders (Gerridae). *Proc. Biol. Sci.* **291**, 20241357 (2024).

41. Zhang, A. M., Li, S. M., Cui, P., Li, S. & Liu, Y. L. A unified theory for bubble dynamics. *Phys. Fluids* **35**, 033323 (2023).

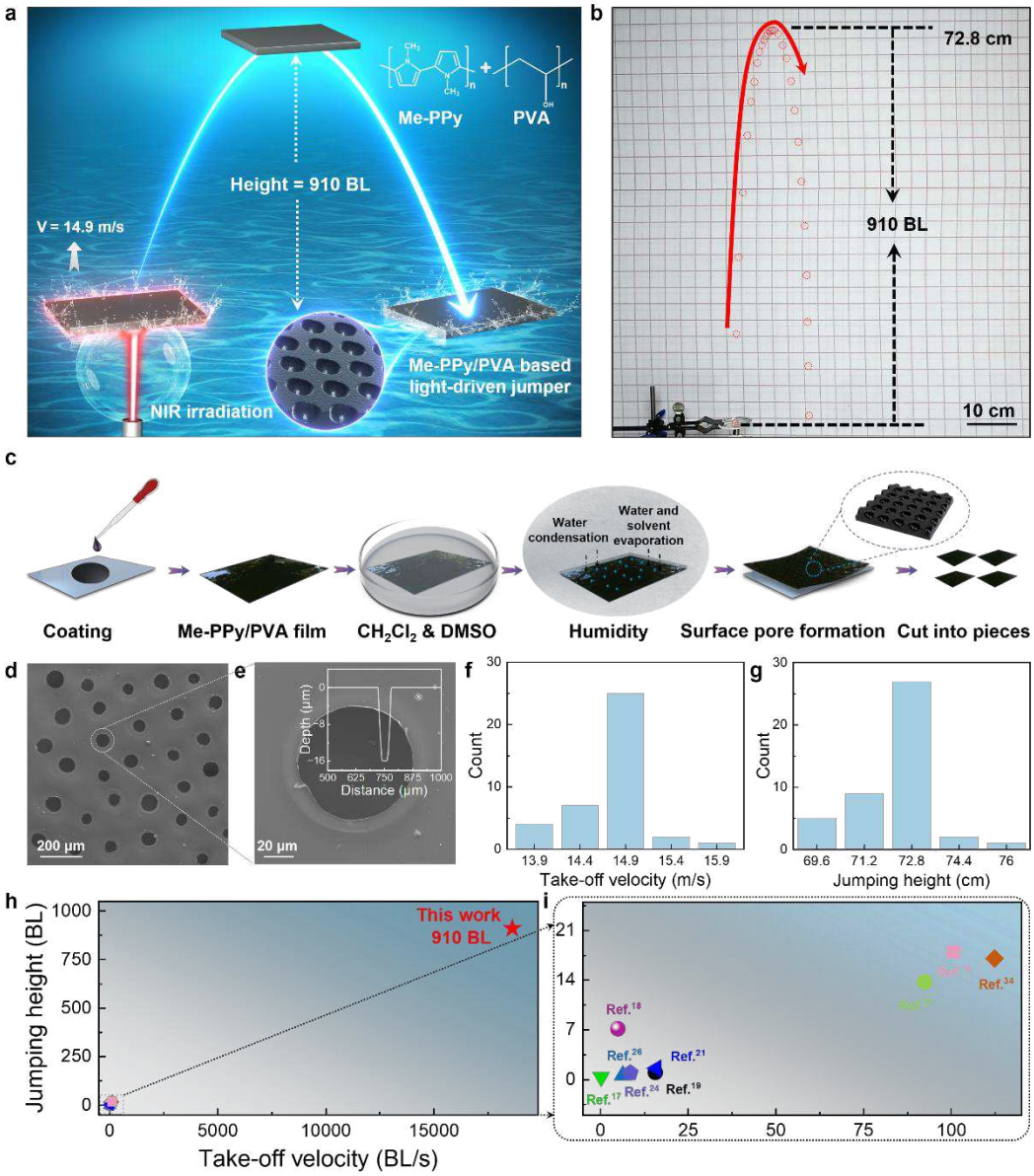


Fig. 1. The light-driven water surface jumper and its jumping performance. (a) Schematic illustration of the light-driven water surface jumping behavior when the jumper is actuated by 1.4 W/cm^2 light. (b) Overlaid camera images (obtained from Supplementary Movie 2) showing the maximum water surface jumping height of the light-driven jumper, where the red curve indicates the jumping direction and the red dashed circles mark the position of the jumper at different periods of time (~0.017 s). (c) Fabrication process of the jumper film consisting of Me-PPy/PVA with surface

micropores using the breath figure method. (d) Scanning electron microscopy (SEM) image indicating the micropores on the surface of the light-driven jumper. (e) The enlarged SEM image of the area marked with the white-dotted circle shown in (d). The inset illustrates the depth of the micropores, which is measured by the profilometer. The take-off velocity and jumping height of the jumper are shown in (f) and (g), respectively. (h) Comparison of the water surface jumping height and take-off velocity between the light-driven jumper in the current study and those reported in the literature. (i) Magnified view of the red dotted rectangle shown in (h).

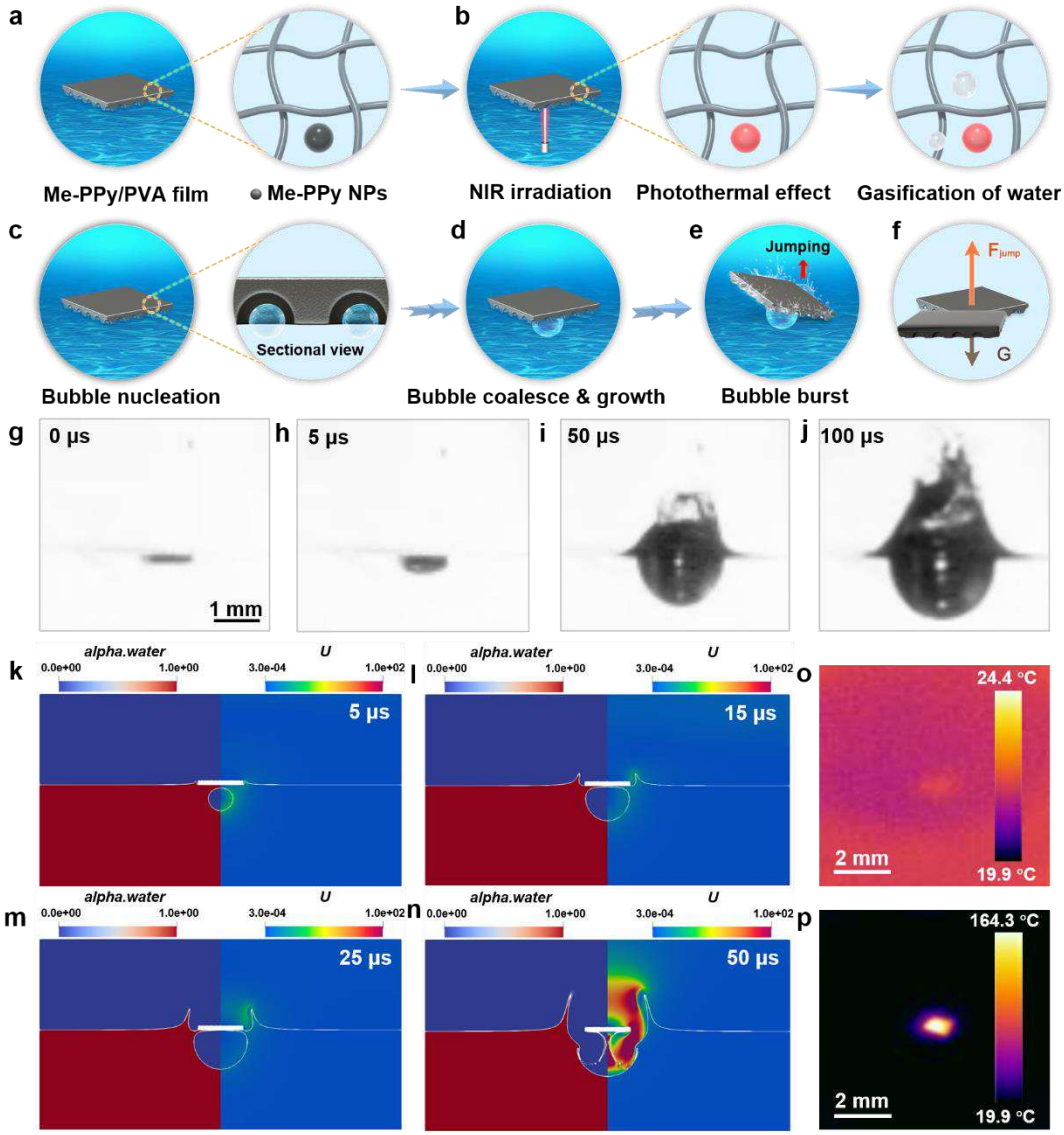


Fig. 2. Jumping mechanism of the light-driven water surface jumper. (a-f) Schematic illustrations depicting the mechanism of the light-driven jumping. (g-j) Time-lapse high-speed camera images (obtained from Supplementary Movie 3) showing the bubble formation, growth and burst processes. (k-n) Simulations showing the bubble growth, superimposed with information on the water volume fraction (*alpha. water*, where 0 indicates pure gas and 1 indicates pure water; left half) and the gas velocity magnitude (*U*, in m/s; right half).

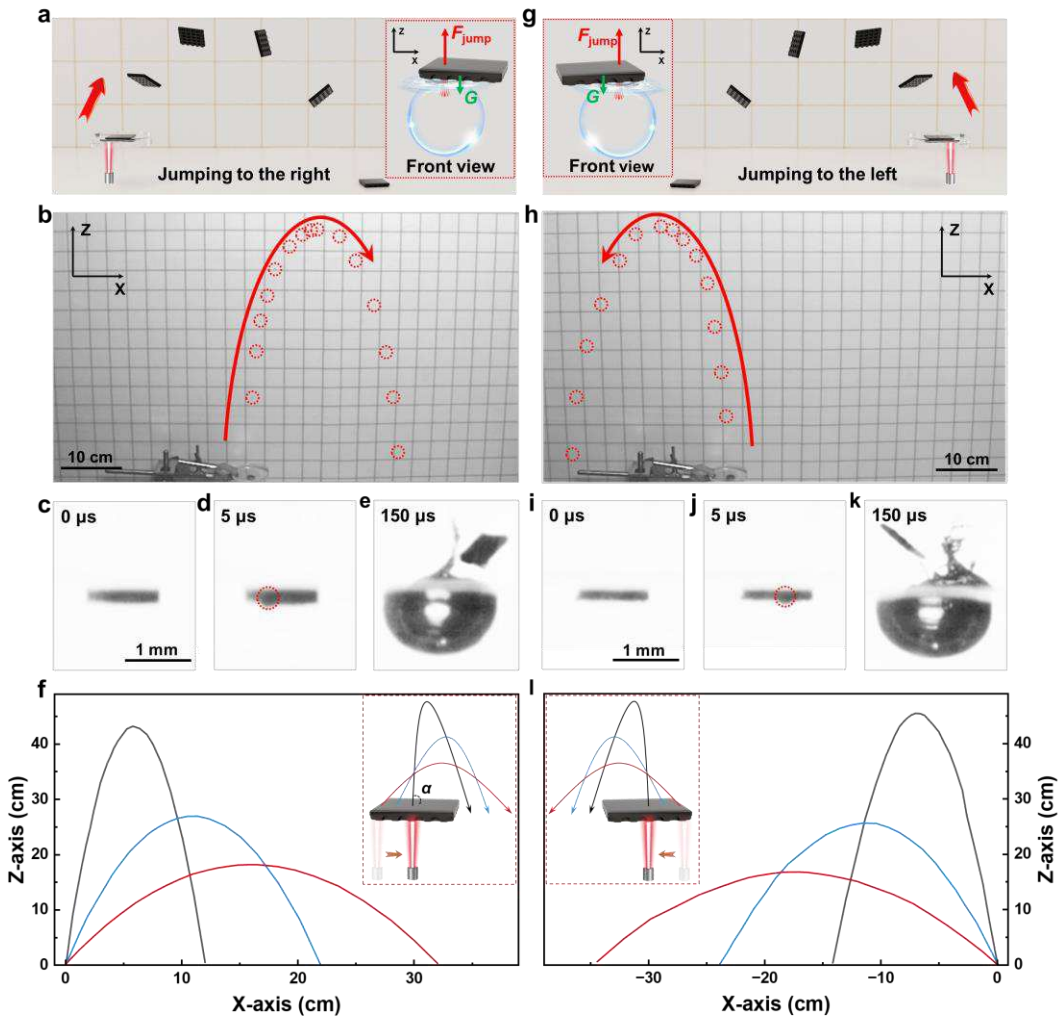


Fig. 3. The control over the jumping behavior of the light-driven water surface jumper. (a) Schematic illustrating the light-driven water surface jumper jumping to the right, which is achieved by irradiating the left half of the jumper. The corresponding force analysis is shown in the inset. (b) Overlaid images of the light-driven jumper jumping to the right, with the red curve denoting the jumping direction and red dashed circles marking the position at different periods of time (0.034 s) (from Supplementary Movie 4). (c-e) High-speed camera images showing the bubble formation (under the left half of the jumper) at the irradiation position which leads to jumping to the right. (f) Trajectories of three light-driven jumpers jumping to the right, realized by

controlling the position of the irradiation center. The insect schematic illustrates the precise regulation of the jumper's take-off angle, jumping height, and horizontal jumping distance. (g) Schematic illustrating the light-driven jumper jumping to the left, which is achieved by controlling the position of the irradiation center. The corresponding force analysis is shown in the inset. (h) Overlaid images of the light-driven jumper moving to the right, with the red curve denoting the jumping direction and red dashed circles marking its position at different periods of time (0.034 s) (from Supplementary Movie 5). (i-k) High-speed camera images showing the bubble formation (under the right half of the jumper) at the irradiation position which leads to jumping to the left. (l) Trajectories of three light-driven jumpers jumping to the left, realized by controlling the position of the irradiation center. The insect schematic illustrates the precise regulation of the jumper's take-off angle, jumping height, and horizontal jumping distance. α in the insets of (f) and (l) denotes the take-off angle. Forces shown in (a) and (g) are as follows: F_{jump} and G are the propulsion force and the gravitational force, respectively.

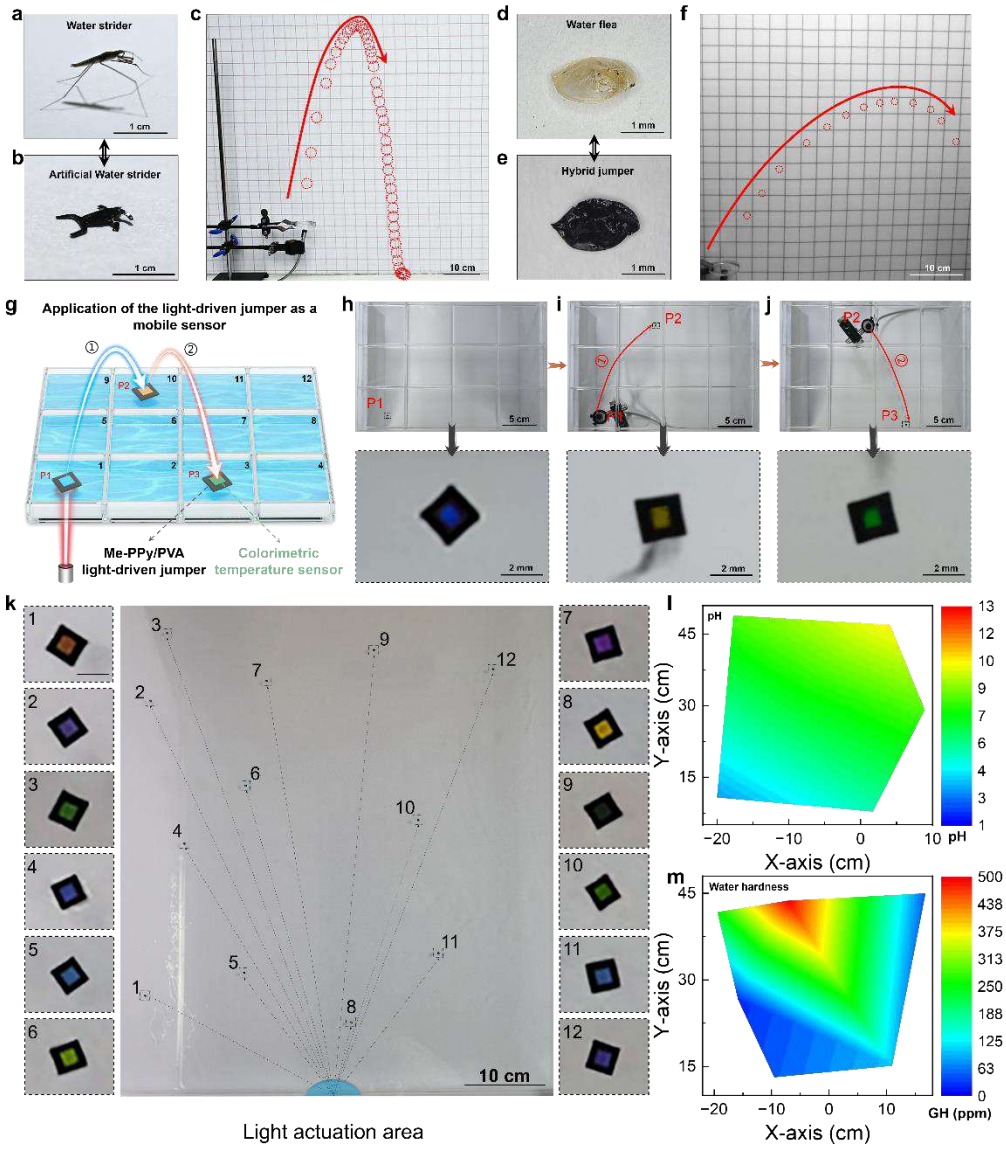


Fig. 4. Potential application demonstration of the light-driven water surface jumper. CCD images of (a) a water strider and (b) the artificial counterpart made of the Me-PPy/PVA composite. (c) Overlaid images showing the trajectory (red circles) of the light-driven jumping motion of the artificial water strider which are captured from Supplementary Movie 6. The red curve indicates the jumping direction and the red dashed circles marking the position at different periods of time (0.017 s). CCD images indicating the shell of a water flea (d) before and (e) after coating with a layer of the Me-PPy/PVA composite. (f) Overlaid images captured from Supplementary

Movie 7 depicting the water surface jumping trajectory (red circles) of the hybrid jumper shown in (e). The red curve illustrates the jumping direction and the red dashed circles marking the position at different periods of time (0.034 s). (g) Schematic showing that the light-driven jumper equipped with a colorimetric temperature sensor can be repeatedly actuated to function as a mobile sensor for acquiring temperature information at different locations. (h-j) Overlaid CCD images of the mobile light-driven jumper equipped with a colorimetric sensor for monitoring environmental temperature at different locations. Enlarged views of the corresponding positions are shown below. The red curve indicates the jumping direction, the red circled number denotes the current excitation number, and P1, P2, and P3 label the corresponding positions. (k) CCD image of distributed light-driven jumpers with attached colorimetric sensors for collective water quality monitoring. The enlarged images at locations from 1 to 12 are also shown. Note that six light-driven jumpers (No. 1, 3, 6, 8, 9, and 10) are equipped with colorimetric pH sensors, while the rest (No. 2, 4, 5, 7, 11, and 12) are equipped with colorimetric water hardness sensors. The scale bar in the enlarged image (No. 1-12) is 2 mm. (l) pH and (m) water hardness distribution in the area indicated in (k) which is obtained by analyzing the color changes of the colorimetric sensors on the surface of light-driven jumpers.

Supplementary Files

This is a list of supplementary files associated with this preprint. Click to download.

- SupplementaryVideo5.mp4
- supportinginformation.pdf
- SupplementaryVideo4.mp4
- SupplementaryVideo3.mp4
- SupplementaryVideo1.mp4
- SupplementaryVideo7.mp4
- SupplementaryVideo2.mp4
- SupplementaryVideo6.mp4